A Laser Scanning Device for Cryogenic Beam Steering at 20 Millikelvin

Jonathan W. Dean, Avirup Roy, Joseph W. Fowler, Kelsey M. Morgan, Sae Woo Nam, Nathan Ortiz, Daniel S. Swetz, Joel N. Ullom, Joel C. Weber, and Galen C. O'Neil

***Abstract*—It is often desirable to steer light within a cryostat and have a well focussed laser spot incident upon a detector. We demonstrate the operation of superconducting transition-edge sensor microcalorimeters with a fiber-coupled laser scanning device colocated on the 20 mK mixing plate of a dilution refrigerator. The scanner directs a 515 nm laser beam with spot size $< 40\ \mu\mathrm{m}$ over a range of ± 14 mm in two orthogonal axes (covering 784 mm^2). We present the optical elements of the system, show that the detector noise spectrum is unchanged when the scanner is operating or OFF, and observe less than 340 nW power dissipation in our use-case. This device will allow detector calibration up to 10 keV on a pixel-by-pixel basis with simultaneous X-ray measurements. Further, this device will enable more effective characterization of certain detector artifacts including crosstalk, position dependences, and drift corrections.**

***Index Terms*—Laser steering, microelectromechanical system (MEMS), superconducting detector, transition-edge sensor (TES), X-ray detector.**

I. Introduction

LASER light is a powerful tool for investigating and manipulating superconducting detectors. Visible and infrared lasers along with a wide range of compatible optical elements to manipulate the beam are readily available from many commercial sources. Commercial wavemeters are available with absolute accuracies exceeding one part in 10^9. Laser light is used at cryogenic temperatures to study photo-induced superconductivity [1], modulate the inductance and resistance of superconducting circuits [2], and move vortices [3]. Applications of scanning lasers include imaging [4] and characterization of position-dependent behavior in superconducting detectors [5]. The application of lasers in sub-100 mK cryogenic environments typical of quantum sensors, qubits, and other quantum devices is limited due to the low cooling power and need for light-tightness. Typically, the moving mechanism that enables scanning is located at a higher temperature stage where cooling power is greater [6]. However, the same path that permits laser radiation to reach quantum devices on the lowest temperature stage may also permit undesired light-leak.

Received 24 September 2025; revised 12 February 2026; accepted 15 February 2026. Date of publication 2 March 2026; date of current version 26 March 2026. This work was supported in part by the U.S. Department of Commerce, National Institute of Standards and Technology under Award 70NANB23H027, in part by the CHIPS Metrology Program, and in part by the CHIPS for America, National Institute of Standards and Technology, U.S. Department of Commerce. *(Corresponding author: Jonathan Dean.)*

Jonathan W. Dean, Avirup Roy, and Joel C. Weber are with the National Institute of Standards and Technology, Boulder, CO 80309 USA, and also with the University of Colorado, Boulder, CO 80309 USA (e-mail: jonathan.dean@nist.gov).

Joseph W. Fowler, Kelsey M. Morgan, Nathan Ortiz, Daniel S. Swetz, Joel N. Ullom, and Galen C. O'Neil are with the National Institute of Standards and Technology, Boulder, CO 80309 USA.

Sae Woo Nam, deceased, was with the National Institute of Standards and Technology, Boulder, CO 80309 USA.

Color versions of one or more figures in this article are available at https://doi.org/10.1109/TASC.2026.3669030.

Digital Object Identifier 10.1109/TASC.2026.3669030

We present a laser scanning apparatus operating on the mixing chamber (MXC) of a dilution refrigerator (DR) at temperatures as low as 16 mK within a light-tight box. We base our design on a capacitively driven MEMS mirror, similar to the work of Stifter et al. [7]. We demonstrate some capabilities of this system by scanning a focussed spot across an array of transition-edge sensor (TES) detectors. We map a single detector showing a large "sweet spot" where pulse response does not vary with location. Also possible with this device is mapping physical detector position with readout channel. Tests are provided showing that the scanner dissipates a small (< 340 nW) amount of power and does not otherwise degrade the performance of the detectors or the DR. This scanner is a versatile tool and we expect that the ability to incorporate laser scanning in light-tight environments at millikelvin temperatures will be valuable for many quantum applications.

Manipulating a highly focussed beam within a cryostat has many potential applications and simultaneously poses several challenges. Steerable optical beams are important in several areas including microscopy, ion/atom manipulation for quantum information, light detection and ranging (LiDAR), among others. Cryogenic particle detectors, such TESs, microwave kinetic inductance detectors (MKIDs), thermal kinetic inductance detectors (TKIDs), and superconducting tunnel junctions (STJs), could all benefit from a steerable and tightly focussed laser pulse. For each of these detectors, and others, optical beam steering offers a method for time-resolved characterization, persistent current switching via thermal [8], [9], and nonthermal [10] means, inductance modulation [2], and position dependence tests of detector responses [11]. Laser annealing is important to the manufacturing of quantum devices and while performed at room temperature, our laser scanner would allow it to be done within the cryostat [12], [13].

Optical laser light has been used previously to calibrate TES and STJ microcalorimeters [14], [15], [16]. Typically, X-ray TES microcalorimeters are calibrated using the values of known X-ray lines and some function that maps between pulse response

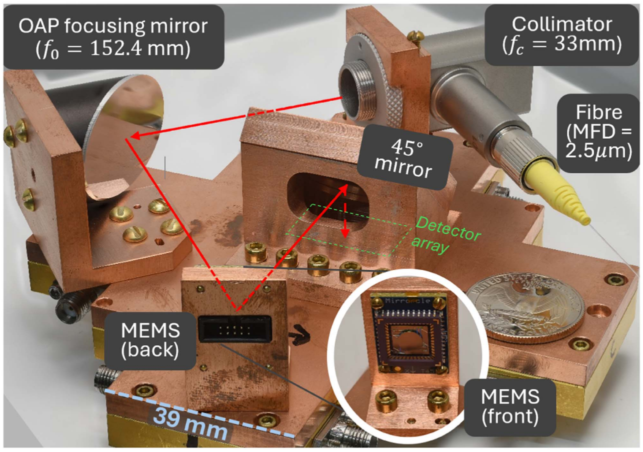

Fig. 1. Laser scanning device showing the optical elements with the red line representing the laser beam path. Dashed lines indicate the element is behind something else. The inset shows a face-on view of the MEMS mirror. A US quarter coin is given for scale along with a scale bar. The detector array is under the 45° mirror, outlined with a green dashed line. This enclosure is placed within a light-tight Al enclosure (not shown).

and energy [17]. The number of calibration points, their uncertainty, the proximity to the X-ray measurement line, and the time between calibration and measurement are all sources of uncertainty in the final measurement. Using optical photons allows for calibration references at each integer multiple of photon energy, leading to vastly more calibration points and greater proximity to the desired measurement line. Moreover, the absolute energy of laser light is known and can be measured to much greater accuracy than X-ray fluorescence lines. In the mentioned studies calibrating TES detectors with laser light [14], [15], [16], they had light incident across the entire detector array, known as flood illumination. With flood illumination, all the detectors are hit simultaneously, causing the maximum amount of detector crosstalk effects. Roy et al. [18] found crosstalk effects exceeding one part per thousand when using flood illumination with the same TES detector array described in this work. Our laser scanning device has a spot size well within the pixel size and can be moved across the detector face for pixel-by-pixel detector calibration which will eliminate crosstalk effects. Furthermore, our device allows for simultaneous X-ray measurements and pulsed-laser calibration.

II. Laser Scanning Device

The laser scanning device, shown in Fig. 1, has been designed and constructed to be compatible with a wide range of cryogenic detectors, electrical circuits, and laser wavelengths. This work will focus on the laser scanner as used with a 4 × 6 array of soft X-ray TES microcalorimeters. Each pixel of the detector array consists of a 250 μm × 250 μm by 250 nm thick Au absorber adjacent to a 30 μm × 90 μm MoAu (47 nm and 700 nm thick) in a “sidecar” geometry [19]. These elements are suspended on 4 μm thick Si_3N_4 membranes upon a larger Si wafer with details in [19]. The detector array sits at the center of a Cu enclosure which also houses a microwave SQUID multiplexer chip and a separate chip with shunt resistors and inductors for the TES circuit. The copper enclosure fits in a 120 mm × 120 mm square and is less than 50 mm tall. The optical elements are mounted on the lid of the enclosure and placed within a light-tight Al enclosure (not shown), which acts as a superconducting magnetic shield. The whole device is placed at the end of a copper scepter attached to the MXC of a horizontal DR.

The laser photons are provided by a green diode laser (515 nm) pulsed with a waveform generator with optical feedthrough into the DR provided by a 200 μm core-diameter multimode fiber. At the MXC, the multimode fiber is adapted to a 2.5 μm core-diameter single-mode fiber with 125 μm cladding-diameter suitable for 450 nm to 600 nm wavelength light. Power loss from coupling a multimode to a single-mode fiber is not a concern in this work due to the low, few-photon, energy range being investigated. The single-mode fiber from the MXC is then coupled to an off-axis parabolic (OAP) mirror collimator with focal length (f_c) of 33 mm (top-right of Fig. 1). The output of our collimator is a 8.58 mm diameter beam (d_0) given by: $d_0 = 2f_c(\text{NA})$, where NA is the numerical aperture of the fiber optic. All beam diameters in this work use the $1/e^2$ definition unless otherwise stated. The collimated beam is incident on a second OAP mirror focuser with a focal length (f_0) of 152.4 mm (top-left of Fig. 1).

The next optical element is the microelectromechanical system (MEMS) mirror from Mirrorcle Tech.[1] is modified for cryogenic purposes and is similar to the mirror used by Stifter et al. [7]. The MEMS mirror is capacitively driven and should therefore dissipate zero power in the steady state [20]. A datasheet is provided [20] to convert the MEMS voltage difference to a mechanical angle on each axis. The maximum voltage difference is ±170 V and the region from –50 V to 50 V is highly linear with 1 V translating to 0.036°. Here, we use these provided values to give values in MEMS mechanical angle or position on the detector face. The reflective surface is a 5 mm diameter bonded mirror with ±5° range of mechanical motion in two perpendicular axes. So far, all optical elements are in the same plane, parallel to the detector enclosure and roughly 20 mm above. The final optical element is the 45° mirror directly above, and sending the beam onto, the detector array. This mirror may be replaced with a thin (0.1 μm to 1 μm) aluminum film to transmit X-rays and filter out infrared light. Prior to the 45° mirror is a hole, which may be covered with indium tin oxide glass, but was left open in the experiments reported here. Alignment pins are used to ensure accurate position and alignment of each optical element. The relevant optical element parameters for this system are given in Table I.

The spot size of the beam at the detector array determines whether we are able to hit single pixels, rather than flood illumination. Spot size, or expected effective beam-width (d_{eff}) of the laser at the focal point is the quadrature sum of the divergence

[1]Certain commercial equipment, instruments, or materials are identified in this article to foster understanding. Such identification does not imply recommendation or endorsement by the National Institute of Standards and Technology, nor does it imply that the materials or equipment identified are necessarily the best available for the purpose.

TABLE I
VALUES OF RELEVANT OPTICAL PARAMETERS

Name	symbol	value
collimator focal length	f_c	33 mm
fiber numerical aperture	NA	0.13
wavelength	λ	515 nm
mode field diameter	d_f	2.5 µm
parabolic mirror focal length	f_0	152.4 mm
MEMS mirror diameter	d_{MEMS}	5 mm
MEMS maximum optical angle	θ_{scan}	$\pm 10°$
Scan range	SR	27.85 mm
expected spot size	d_{eff}	25.13 µm

limited, d_{div}, and diffraction limited, d_{diff}, spot sizes

$$d_{\text{eff}} = \sqrt{d_{\text{diff}}^2 + d_{\text{div}}^2} \quad (1)$$

with

$$d_{\text{diff}} = \frac{2 \times 1.22\lambda f_0}{d_0}, \; d_{\text{div}} = \frac{d_f f_0}{f_c}. \quad (2)$$

With the optical elements from Table I we have a diffraction limited spot size of 22.32 µm, a divergence limited spot size of 11.55 µm, and an effective spot size of 25.13 µm. These parameters give a spot size well within our 250 µm square pixel absorber.

The detector array covers 14 mm × 7 mm with the MEMS mirror neutral state aimed at the center of the array. The full scan range, SR, of the optical path is limited by the optical angular extent (twice the mechanical extent) of the MEMS mirror (θ_{scan}) and the distance from the MEMS to the array (L_{scan}) along the beam path

$$\text{SR} = 2L_{\text{scan}}\tan(\theta_{\text{scan}}). \quad (3)$$

To reach each pixel of this detector, the MEMS mirror must be at least 40 mm from the detector array. Due to concerns of possible scan range deterioration in the cryogenic state and the desire to use larger detectors in the future, we have almost doubled this required distance and placed the MEMS mirror 78.98 mm from the detector, allowing for a full scan range of 27.85 mm (±13.93 mm) across two perpendicular axes. In fact, it seems as though the cryogenic environment may increase the scan range of the MEMS mirror [21], which we observed in our tests, discussed later with reference to Fig. 8.

The distance between the parabolic focusing mirror and the MEMS mirror is $z_{\text{MEMS}} = f_0 - L_{\text{scan}} = 73.42$ mm where z is the distance along the optical path from the focusing element. The beamwidth, $w(z)$, at the MEMS mirror is 4.45 mm, from

$$w(z) = \frac{4f_0\lambda M^2}{\pi d_0}\sqrt{1 + \frac{4(z-f_0)^2}{(\text{DoF})^2}}\,, \; \text{DoF} = \frac{8\lambda M^2 f_0^2}{\pi d_0^2} \quad (4)$$

where λ is wavelength, DoF is the depth of field, and M^2 is beam-quality. We approximate $\text{M}^2 = 1$ due to the use of single-mode fiber. The angle between the MEMS mirror normal vector and the beam path is 22.5° for the MEMS mirror neutral position, resulting in the Gaussian laser profile effectively being incident on an ellipse with semimajor and semiminor radii of $a = 2.5$ mm and $b = 2.22$ mm, respectively. The power of a Gaussian beam outside this ellipse is

$$\frac{P_{\text{out}}(z)}{P_{\text{tot}}(z)} = \int\int_{\frac{x^2}{a^2}+\frac{y^2}{b^2}\le 1} dxdy\frac{2}{\pi w^2}\exp\left(-2\frac{x^2+y^2}{w(z)^2}\right). \quad (5)$$

The integral is solved numerically and gives a power loss at the MEMS mirror of 10.4%. Power incident outside the mirror is reflected and may reach the sensors. Some applications may choose to reduce the power outside the MEMS mirror by increasing z_{MEMS}, which will necessarily decrease the scan range, L_{scan} for a fixed f_0. Another design tradeoff is between scan range and spot size, demonstrated by rearranging (1) and (2) with parameters from Table I

$$d_{\text{eff}} = \frac{f_0}{f_c}\sqrt{\left(\frac{1.22\lambda}{(\text{NA})}\right)^2 + d_f^2} \quad (6)$$

which shows linear proportionality between spot size and focal length ($d_{\text{eff}} \propto f_0$). The focal length expressed in terms of distances L_{scan} and z_{MEMS} is $f_0 = L_{\text{scan}} + z_{\text{MEMS}}$, which is substituted into (6), and using the definition (3) gives

$$d_{\text{eff}} = \left(\frac{\text{SR}}{2f_c\tan(10°)} + \frac{z_{\text{MEMS}}}{f_c}\right)\sqrt{\left(\frac{1.22\lambda}{(\text{NA})}\right)^2 + d_f^2}. \quad (7)$$

For the chosen $z_{\text{MEMS}} = 73.42$ mm, we obtain

$$d_{\text{eff}} = 0.4675\ \text{SR} + 12.10\ (\mu\text{m}). \quad (8)$$

Highlighting the tradeoff between spot size and scan range.

III. RESULTS

Results are presented on spot size measurements at room-temperature, power dissipation, detector readout noise, photon detection and detector characterization, and cryogenic measurements of spot size.

A. Room-Temperature Spot Size

The spot size was measured by placing a CCD camera at the same distance from the MEMS mirror as the detector array would be. The CCD contains an array of 3.45 µm × 3.45 µm square pixels. An histogram is obtained from the intensity along the row of pixels that gives the largest spot size. A constant background and Gaussian profile are fitted to the histogram and result in an FWHM of 20.72 µm ± 3.45 µm (see Fig. 2). Converting FWHM to a $1/e^2$ definition of beam width, d, gives a spot size of 35.20 µm ± 5.90 µm, from

$$d = \text{FWHM}/\sqrt{2\ln(2)}. \quad (9)$$

Measurements were also performed in the cryostat while cold, discussed in Section III-E.

B. Cryogenic Power Dissipation

Power dissipated by moving elements can be a challenge in cryogenic environments. In a DR the cooling power at 15 mK is typically of order 1 µW while in adiabatic demagnetization refrigerators 1µW may be a significant power load even at

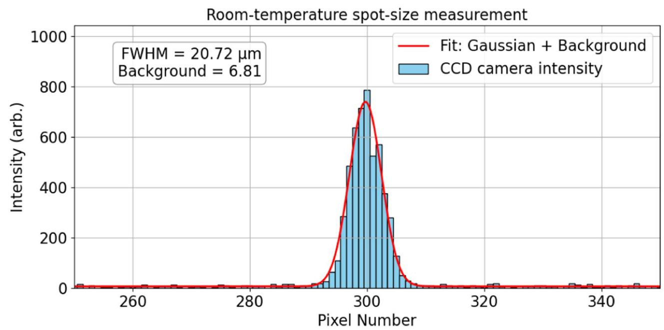

Fig. 2. Room temperature spot size measurement with a CCD camera with 3.45 µm × 3.45 µm square pixels. The histogram comes from a slice at the widest part of the beam.

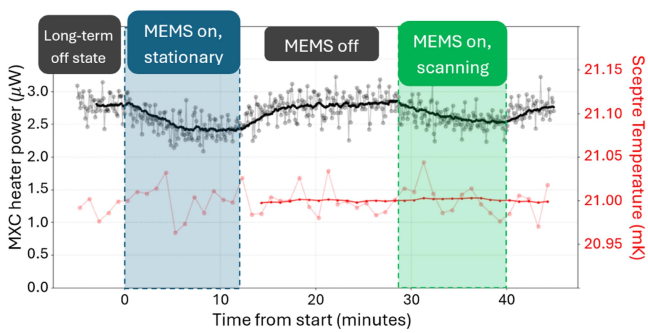

Fig. 3. Raw power dissipated (left y-axis) by the MXC heater to regulate at 21 mK. The light colored points are regulation heater power (black) and temperature at the laser scanner (red) with the 20-event-averaged data in dark color. The shaded regions are when the MEMS are, first, turned ON and stationary at position (0°, 0°), second, during a scan. Only the last quarter of the data during these regions is taken to obtain average power dissipation once the power is stable.

100 mK. The laser scanner is on the end of a scepter attached to the MXC and we measure the temperature there, approximately 16 mK at base. We operate at 21 mK using proportional–integral–derivative (PID) feedback to regulate and observe a root-mean-square variation of 16 µK with mean power dissipation from the heaters of 2.83 µW.

The MEMS has been tested in three different "ON" settings: centered, stationary at (0°, 0°); offset, stationary at (5°, 5°); and scanning. The scanning procedure is important later in imaging an individual pixel (see Fig. 5) and is explained: the MEMS moves the laser to a point, waits for 0.2 s allowing for any controller delay [20]; then the laser is pulsed with 16 ns wide pulses every 10 ms (100 Hz) for 0.5 s; last, the MEMS controller output is shut OFF for 0.3 s, then moves to a new point and repeats. This power cycling prevented some arbitrary and unwanted behavior where the mirror would occasionally jiggle around some (x, y) position. We believe this arises because the total capacitance of our wiring exceeds the specified maximum capacitance of the MEMS controller and have plans to amend this in future work. During the "ON" state, the laser is outputting less than 1 fW of power. Fig. 3 presents the MXC heater power as a function of time for the "OFF," "centered," and "scanning" settings while regulating at 21 mK. With the MEMS "OFF" the

TABLE II
MEMS Power Dissipation in Three States: Centered, Stationary At (0°, 0°); Offset, Stationary At (5°, 5°); and Scanning

State	MEMS power (µW)
Centred	0.32
Offset	0.34
Scanning	0.29

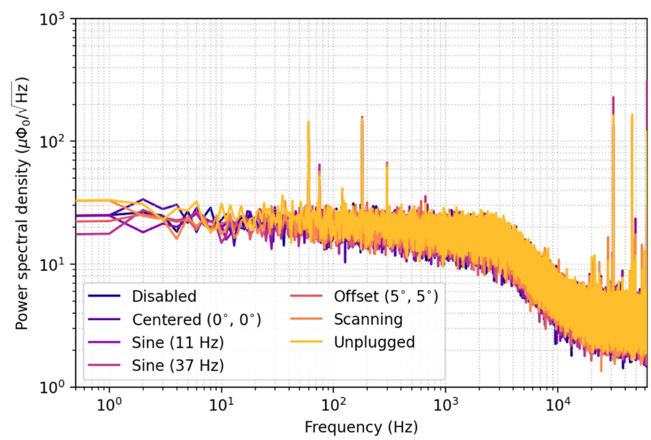

Fig. 4. Detector noise spectral density measurements for a single biased pixel at different MEMS settings. No noticeable difference was observed during the different MEMS settings.

mean power dissipated from the MXC heater is 2.83 µW, from data across an hour before the start of the data in Fig. 3. The quantitative values for power dissipation are given in Table II and are found from taking the difference in the MXC heater power from the "OFF" state (2.83 µW) and the mean power dissipated in the last quarter of the "ON" or "scanning" periods to allow for the heater power to settle. We find that the MEMS power dissipated is no more than 0.34 µW at the three tested setting, with all three being roughly equal.

C. Impact on Detector Noise

Noise measurements on 0.34 V biased detectors were performed with the MEMS "OFF," at each of the three "ON" settings described previously, as well as scanning the mirror sinusoidally at 11 Hz and 37 Hz. These values are arbitrary prime numbers with higher frequency than our typical use case. The results are presented in Fig. 4 with no significant noise observed from any of the settings.

D. Laser Photon Detection

The TES microcalorimeter array in this work is typically used for soft X-ray detection and has not been modified in any way to work with optical photons. The laser used here is a 515 nm (2.4 eV) green laser and is pulsed with a function generator, varying the width of each pulse and with physical attenuators we are able to reach the desired photon numbers absorbed on the detector. The scanning procedure from earlier, but with dwell time reduced to 0.3 s (30 total laser pulses), is used to create the heat map in Fig. 5(a). For these scans, we are in the single

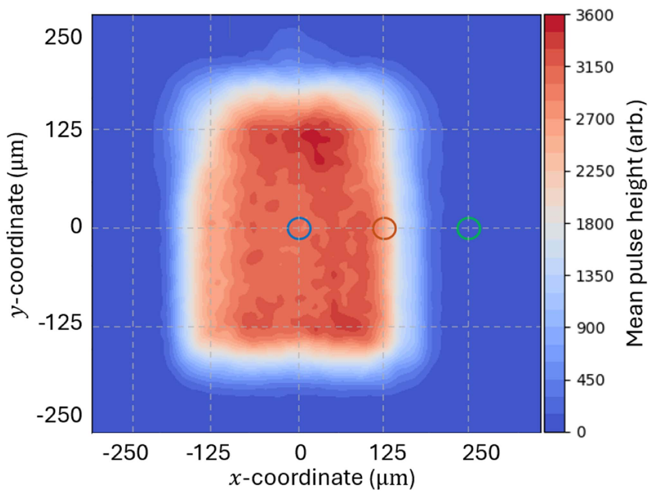

(a)

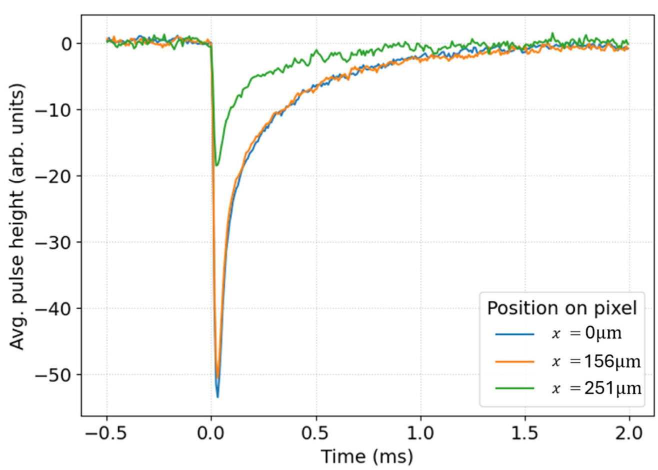

(b)

Fig. 5. Heatmap imaging a single TES absorber and selected individual pulse traces at three different locations. (a) Heat-map of median pulse-height as the laser is scanned across a TES microcalorimeter pixel. Three circles are shown at $y = 0$ μm and $x = 0$ μm, 126 μm, 251 μm, for the origin set to the centre of the pixel, which are the locations of the pulse traces below. (b) Three pulse traces from the locations above. For the "offabsorber" pulse (green, $x = 251$ μm) the majority of events are indistinguishable from noise, we selected an event with a pulse for display.

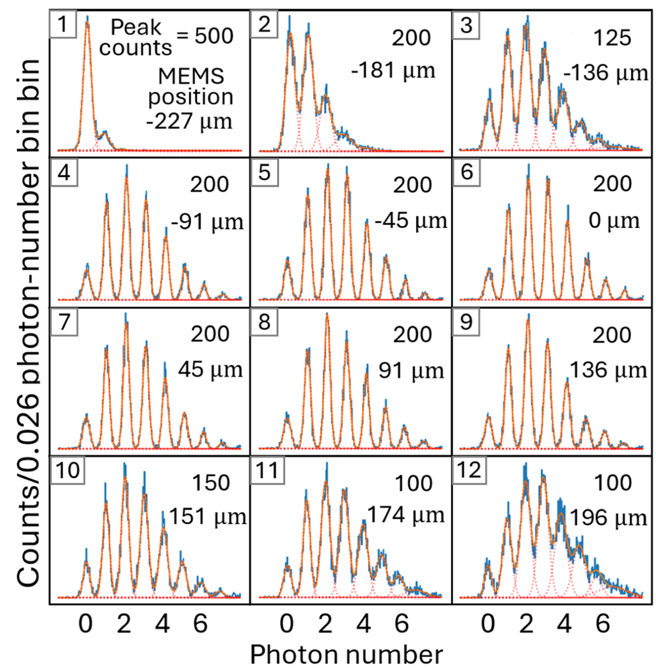

Fig. 6. Histograms of counts (y-axis) per 0.025 photon-number bin versus photon-number (x-axis) for twelve different points along the vertical-axis on the TES pixel shown in Fig. 5(a). Raw data is blue, with a fit of seven Gaussians overlaid in orange. The top value in each cell is the number of counts at the top of the y-axis, the lower value is the MEMS coordinate y-axis value in microns where the center of the absorber is the origin.

photon regime, with a mean photon number, n, of approximately three arriving in each pulse. These pulses are quite small and difficult to discern from noise, therefore we trigger the data acquisition software with each pulse and do not rely on some pulse triggering algorithm. We clearly resolve the shape of the detector and membrane. There is a sharp decrease in pulse-height as the laser is aimed toward the edge of the absorber and on the membrane (light-blue). Occasionally, small pulses are observed when the laser is aimed off the absorber (dark-blue), possibly due to reflected photons that reach the detector membrane. The TES is attached above (positive y) the absorber in "side-car" geometry [19] which is seen here with the stretching-out of the heat-map in the positive y-axis. Three circles along the y-axis are shown and a representative pulse from those locations is given in Fig. 5(b). There is great consistency between pulses on the edge of the absorber, $x = 156$ μm, and the center of the absorber, $x = 0$ μm. The pulse on the Si wafer at $x = 251$ μm is much smaller and only occurs for roughly one in ten laser pulses, with the rest being indistinguishable from noise, we have chosen one of these pulses to report in Fig. 5(b). We believe the small differences in mean pulse-height on the absorber in Fig. 5(a) are from Poissonian variations in laser output power, which should have a mean and variance of 90 for the 30 events.

As the laser is driven across the absorber, we are able to achieve single photon resolution of the detector with 515 nm photons, shown in Fig. 6. We expect n laser generated photons of energy E_n will result in an identical pulse as if a single photon of energy $n \times E_n$ were absorbed. This is a safe assumption as the 10% to 90% rise time of these pixels is 12 μs [19], significantly longer than the 16 ns laser pulsewidth. Pulses are recorded in filtered pulse-height units [22], which are then converted to photon-number units by using the centroid of the single photon peak. Fig. 6 presents the counts per 0.025 bin of photon-number units as the laser is moved across the absorber along the y-axis. For this scan the dwell time is increased to allow for roughly 5000 events at each location. The first frame shows that when the laser is aimed off the membrane, most pulses fall into the "zero photon peak." When the laser is aimed at the edge of the absorber and significantly on the membrane, as in panels two and three, then 11 and 12 show that multiple photon peaks are visible, however, the resolution is quite poor. When the laser is aimed at the Au absorber, as in panels four to ten, there is great consistency between the collected histograms. In total,

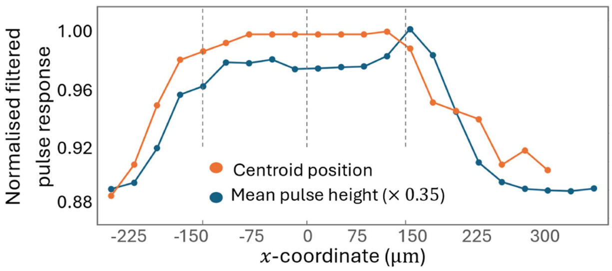

Fig. 7. Detector characteristics as the laser is scanned across the x-axis. The center of single-photon peak is the centroid of the Gaussian in the second peak of Fig. 6. For both measures, the flatness of the central region indicates a large area with no position dependence. The dashed lines indicate the center of the absorber and the edges of the membrane on each side, 135 μm from the center.

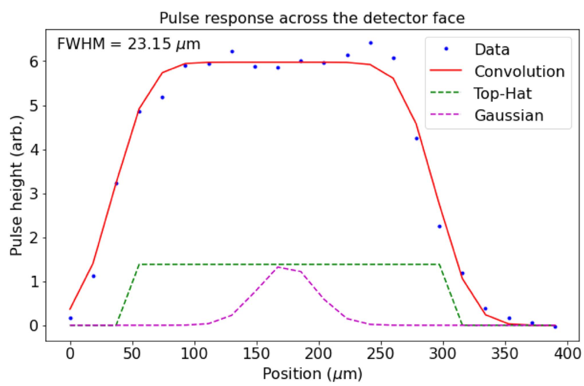

Fig. 8. Convolution of a top-hat and Gaussian fit to the median pulse-height data during a scan across the x-axis. The low sampling rate results in the misshapen Gaussian and top-hat function.

27 different locations were recorded in an x-axis scan with all data supporting the trends observed in the 12 locations from Fig. 6. The single photon peak shows a resolution of 0.8 eV averaged across the 18 locations on the absorber and events up to eight-photon peaks are observed.

Fig. 7 shows the center of the single-photon peak as the laser scans across the x-axis. The center of the single-photon peak is determined by the centroid of the Gaussian used to fit the second peak in Fig. 6. Also shown in Fig. 7 is the mean pulse-height. Both metrics show a region of very consistent detector response.

E. Cryogenic Spot Size

The room temperature direct measurement of spot size with a CCD camera achieved a spot size of 35.20 μm ± 5.90 μm (see Fig. 2). A second measurement was done in the cryogenic state by scanning the beam across one of the 250 μm wide Mo/Au absorbers [see Fig. 5(a)]. The 10 μm wide membrane on each side of the absorber has a pulse response and is included in the model. The ideal response on a perfect absorber from an arbitrarily small laser width is a top-hat function. The laser spot is modeled as a Gaussian. Therefore, the median pulse-height response as a function of laser position across the pixel is appropriately modeled as the convolution between a Gaussian with FWHM, σ, and a top-hat with width, $\hat{w} = 270$ μm. This convolution is the sum of two error functions

$$f(x) = \frac{A_0}{2\hat{w}}\left[\mathrm{erf}\left(\frac{x+\hat{w}}{\sqrt{2}\sigma}\right) - \left(\frac{x-\hat{w}}{\sqrt{2}\sigma}\right)\right] \tag{10}$$

where A_0 is a normalizing constant. The convolution is fitted to the data from a horizontal slice from Fig. 5(a) at $y = 0.33$ μm. The result of this fit is presented in Fig. 8. The Gaussian FWHM is $\sigma = 23$ μm, or, beam width (1/e^2) of 39 μm ± 3 μm. For Fig. 8, the voltage-to-position conversion is done through fitting a top-hat function with fixed width. Using the MEMS mirror data sheet for this conversion and having the top-hat function width as a free parameter provides an absorber plus membrane width of 284 μm ± 4 μm width. This supports a previous finding from Stifter et al. [21] where the mechanical angle of the MEMS increases for the same voltage difference applied.

F. X-Ray Filter as the 45° Mirror

One of the features of our design is that the 45° mirror may be swapped with a thin aluminum foil that is permeable to X-rays. This operates as an optical/X-ray dichroic beam splitter and enables simultaneous calibration and X-ray detection. During this operation, a similar Al foil is placed in the light-tight Al enclosure that surrounds the scanner from Fig. 1 so there is line-of-sight for X-rays from some source to the detector array with the enclosure remaining light-tight. The soft X-ray filter is a 25.4 mm diameter, 116 nm thick aluminum foil layered on a ≈25 μm thick polymer. The filter is not designed to be used as an optical mirror, however, it is capable of performing well-enough for our purposes since the laser spot size remains within the pixel size. Using the convolution methods from the previous section, the infrared filter being used as a mirror results in a 1/e^2 spot size of ≈ 70 μm. This is significantly smaller than our absorber size allowing for single-pixel calibration with simultaneous X-ray measurements.

IV. Conclusion

In this work, we have demonstrated the ability to focus a laser beam to ≈ 35 μm spot size and scan over an array of detectors on detectors mounted on the MXC of a DR. We have imaged a single pixel using the pulse response as the laser is scanned across it in two axes. We observed no impact on detector noise. The ability to regulate at 21 mK has been demonstrated with the MEMS dissipating roughly 0.3 μW in three different settings. We plan to use this device in combination with a significantly upgraded laser setup to perform high accuracy TES energy calibration on a pixel-by-pixel basis, avoiding any impacts of crosstalk. With 400 nm photons of 3 eV, and based on state of the art multiplexed X-ray microcalorimeter energy resolutions of 2.33 eV at 8 keV [23], we expect this method of calibration to be viable for X-rays of at least 10 keV.

The ability to scan a focussed laser spot in a light-tight box is a versatile tool for manipulating and studying low temperature detectors. We expect to continue to use this laser scanner for crosstalk-free TES array calibration, characterizing position dependence, crosstalk evaluation, and mapping resonator frequency to physical position. It may also serve as a more flexible replacement for the large LED arrays used for kinetic inductance detector position mapping [24]. Already, this laser scanner has been used in two other experiments with results to be published simultaneously: for directing the laser to drive segments of a superconducting circuit normal, acting as a persistent current switch [25]; and for mapping position dependence on a thermal kinetic inductance detector [26]

Acknowledgment

The authors would like to thank K. Stifter and N. Kurinsky for their help with the setting up of the MEMS mirror.

References

[1] A. Cavalleri, "Photo-induced superconductivity," *Contemporary Phys.*, vol. 59, no. 1, pp. 31–46, 2018.

[2] S. W. Nam, G. S. Park, B. Cabrera, and M. E. Huber, "Optically induced inductance modulation of a Nb coil," *Proc. SPIE*, vol. 2160, pp. 187–194, 1994.

[3] S. E. Lillie et al., "Laser modulation of superconductivity in a cryogenic wide-field nitrogen-vacancy microscope," *Nano Lett.*, vol. 20, no. 3, pp. 1855–1861, 2020.

[4] A. Sivakov, A. Zhuravel', O. Turutanov, and I. Dmitrenko, "Spatially resolved characterization of superconducting films and cryoelectronic devices by means of low temperature scanning laser microscope," *Appl. Surf. Sci.*, vol. 106, pp. 390–395, 1996.

[5] X. Liu et al., "Cryogenic led pixel-to-frequency mapper for kinetic inductance detector arrays," *J. Appl. Phys.*, vol. 122, no. 3, 2017, Art. no. 034502.

[6] A. Kittel, P. Stagge, and J. Parisi, "Scanning-laser microscope for cryogenic applications," *Rev. Sci. Instrum.*, vol. 68, no. 2, pp. 1286–1290, 1997.

[7] K. Stifter et al., "Cryogenic optical beam steering for superconducting device calibration," 2024, *arXiv:2405.02258*.

[8] T. Francavilla, H. Nelson, A. Baronavski, S. Wolf, D. Gubser, and R. Hein, "Further studies of a laser quenched superconducting opening switch," *IEEE Trans. Magn.*, vol. 25, no. 2, pp. 1996–1999, Mar. 1989.

[9] F. Ayela, J. Bret, and J. Chaussy, "High frequency thermal modulation of superconducting NbTi thin film by use of laser diode," *Cryogenics*, vol. 34, no. 7, pp. 597–601, 1994.

[10] L. R. Testardi, "Destruction of superconductivity by laser light," *Phys. Rev. B*, vol. 4, pp. 2189–2196, 1971.

[11] D. Yan, L. M. Gades, T. Guruswamy, U. M. Patel, O. Quaranta, and A. Miceli, "Modelling a transition-edge sensor X-ray microcalorimeter linear array for compton profile measurements and energy dispersive diffraction," *IEEE Trans. Appl. Supercond.*, vol. 29, no. 5, Aug. 2019, Art. no. 2100804.

[12] J. B. Hertzberg et al., "Laser-annealing Josephson junctions for yielding scaled-up superconducting quantum processors," *NPJ Quantum Inform.*, vol. 7, no. 1, 2021, Art. no. 129.

[13] H. Kim et al., "Effects of laser-annealing on fixed-frequency superconducting qubits," *Appl. Phys. Lett.*, vol. 121, no. 14, 2022, Art. no. 142601.

[14] F. Ponce, E. Swanberg, J. Burke, R. Henderson, and S. Friedrich, "Accurate measurement of the first excited nuclear state in ^{235}U," *Phys. Rev. C*, vol. 97, 2018, Art. no. 054310.

[15] F. T. Jaeckel et al., "Energy calibration of high-resolution X-ray TES microcalorimeters with 3eV optical photons," *IEEE Trans. Appl. Supercond.*, vol. 29, no. 5, Aug. 2019, Art. no. 2100104.

[16] S. Zhang, J. Xia, and B. Wu, "A calibration system adopting 405 nm laser for soft x-ray TESs," in *Proc. 8th Symp. Novel Photoelectronic Detection Technol. Appl.*, 2022, Art. no. 69.

[17] J. W. Fowler et al., "Absolute energies and emission line shapes of the l X-ray transitions of lanthanide metals," *Metrologia*, vol. 58, no. 1, 2021, Art. no. 015016.

[18] A. Roy et al., "Characterization of silicon-membrane TES microcalorimeters for large-format X-ray spectrometers with integrated microwave squid readout," *IEEE Trans. Appl. Supercond.*, vol. 36, no. 6, Sep. 2026, Art. no. 2100608.

[19] J. C. Weber et al., "Development of a transition-edge sensor bilayer process providing new modalities for critical temperature control," *Superconductor Sci. Technol.*, vol. 33, no. 11, 2020, Art. no. 115002.

[20] Mirrorcle Technologies, Inc., "Mirrorcle technologies MEMS mirrors—Technical overview," 2017. Accessed: Jul. 3, 2025. [Online]. Available: https://www.mirrorcletech.com/wp/wp-content/uploads/2018/01/Mirrorcle-Technologies-MEMS-Mirrors-Technical-Overview.pdf

[21] K. Stifter and N. Kurinsky, "Personal communication," 2025.

[22] J. W. Fowler et al., "The practice of pulse processing," *J. Low Temp. Phys.*, vol. 184, no. 1, pp. 374–381, 2016.

[23] S. J. Smith et al., "Performance of a broad-band, high-resolution, transition-edge sensor spectrometer for x-ray astrophysics," *IEEE Trans. Appl. Supercond.*, vol. 31, no. 5, Aug. 2021, Art. no. 2100806.

[24] J. E. Shroyer, M. Nelson, L. Walters, and B. R. Johnson, "A scalable cryogenic led module for selectively illuminating kinetic inductance detector arrays," *Rev. Sci. Instrum.*, vol. 93, no. 11, 2022, Art. no. 113107.

[25] A. Roy et al., "Addressing individual persistent-current switches with a cryogenic optical scanner," *IEEE Trans. Appl. Supercond.*, early access, Mar. 6, 2026, doi: 10.1109/TASC.2026.3671158.

[26] I. F. Florang et al., "A study of the position-dependent response of thermal kinetic inductance detectors through the use of cryogenic beam steering," presented at the Low-Temperature Quantum Detectors Conf., Helsinki, Finland, Aug. 3-6, 2025.